

## The efficiency of electron acceleration by ICME-driven shocks

G. QIN,<sup>1</sup> F.-J. KONG,<sup>2,1</sup> AND S.-S. WU<sup>1</sup>

<sup>1</sup>*School of Science, Harbin Institute of Technology, Shenzhen, 518055, China; qingang@hit.edu.cn*

<sup>2</sup>*School of Physics and Electronics, North China University of Water Resources and Electric Power, Zhengzhou, 450046, China;  
kongfanjing@ncwu.edu.cn*

### ABSTRACT

We present a study of the acceleration efficiency of suprathermal electrons at collisionless shock waves driven by interplanetary coronal mass ejections (ICMEs), with the data analysis from both the spacecraft observations and test-particle simulations. The observations are from the 3DP/EESA instrument onboard *Wind* during the 74 shock events listed in Yang et al. 2019, ApJ, and the test-particle simulations are carried out through 315 cases with different shock parameters. It is shown that a large shock-normal angle, upstream Alfvén Mach number, and shock compression ratio would enhance the shock acceleration efficiency. In addition, we develop a theoretical model of the critical shock normal angle for efficient shock acceleration by assuming the shock drift acceleration to be efficient. We also obtain models for the critical values of Mach number and compression ratio with efficient shock acceleration, based on the suggestion of Drury 1983 about the average momentum change of particle crossing of shock. It is shown that the theories have similar trends of the observations and simulations. Therefore, our results suggest that the shock drift acceleration is efficient in the electron acceleration by ICME-driven shocks, which confirms the findings of Yang et al.

Corresponding author: G. Qin  
qingang@hit.edu.cn

*Keywords:* acceleration of particles–shock waves–Sun: coronal mass ejections (CMEs)

## 1. INTRODUCTION

Electron acceleration is a vital topic in space and astrophysical plasmas. The well-known efficient accelerators are collisionless shocks which are able to accelerate electrons to high energies. It is widely accepted that diffusive shock acceleration (DSA; [Axford et al. 1977](#); [Krymsky 1977](#); [Bell 1978](#); [Blandford & Ostriker 1978](#)), i.e., the combination of FFA and SDA, remains the dominate particle acceleration mechanism at collisionless shocks. Recently many authors have studied the acceleration of electrons. [Tsuneta & Naito \(1998\)](#) proposed that in solar flares the formation of an oblique fast shock below the reconnection region provides the acceleration site for nonthermal electrons of 20–100 keV by first-order Fermi acceleration (FFA) mechanism. [Guo & Giacalone \(2012\)](#) studied electron acceleration at the flare termination shock in large-scale magnetic fluctuations and found that electrons can be accelerated to a few MeV which can qualitatively explain the observed hard X-ray emissions. [Mann et al. \(2001\)](#) suggested that, in the solar corona, high energetic electrons of 1 MeV can be produced by shock waves if strong magnetic field fluctuations appear near the shock transition so electrons are allowed to cross the shock front many times by field-line meandering. [Klassen et al. \(2002\)](#) investigated the origin of 0.25–0.7 MeV electrons in solar energetic particle events through observations from COSTEP/*SOHO* and *Wind* 3DP instruments and concluded that the electrons measured are accelerated by coronal shock waves. [Mann et al. \(2006\)](#) suggested that hard X- and  $\gamma$ -rays can be generated by electrons that are accelerated by shock drift acceleration (SDA) mechanism at the termination shock during solar flares. [Warmuth et al. \(2009\)](#) developed a quantitative model based on radio and hard X-ray observations to study the acceleration of electrons in solar flares, and showed the possibility of shock drift acceleration at the reconnection outflow termination shock. In addition, [Miteva & Mann \(2007\)](#) proposed that in the solar corona energetic electrons at quasi-perpendicular shocks can be accelerated by resonant whistler wave-electron interaction. [Saito & Umeda \(2011\)](#) performed particle-in-cell simulations for electron acceleration at a quasi-perpendicular shock, and showed that the parallel scattering by the kinetic Alfvén turbulence, which is generated in the shock transition, suppresses the reflection of electrons during the shock drift acceleration process.

Dresing et al. (2016) determined the particle acceleration efficiency at interplanetary shock crossings observed by *STEREO* spacecraft, and found that only 1% (five events) of all analyzed shocks shows a shock-associated electron intensity increase for 65–75 keV electrons. Among the five events, they found that four were associated with ICME-driven quasi-perpendicular shocks and the rest one was associated with an SIR<sup>1</sup> (with an ICME embedded in) forward quasi-parallel shock. It is possible that the observed shock-associated electron intensity increase events have more occurrence frequency in quasi-perpendicular than in quasi-parallel shocks, although there is very poor statistics in their studies. Furthermore, Yang et al. (2018) studied the acceleration of suprathermal electrons in the energy range of 0.3–40 keV at an ICME-driven quasi-perpendicular shock with the spacecraft observations, and obtained the 90° pitch angle enhancements and larger downstream electron spectral index. In the statistical work of Yang et al. (2019), for those selected quasi-perpendicular and quasi-parallel shock events they found a positive correlation between the average downstream suprathermal electron flux and magnetosonic Mach number, and the downstream flux enhancement and magnetic compression ratio. These results imply the importance of shock drift acceleration in the acceleration of electrons at quasi-perpendicular shocks. Furthermore, Yang et al. (2019) suggested that there are more SEP events associated with quasi-perpendicular shocks compared to quasi-parallel shocks.

In the previous work (Kong & Qin 2020), using test-particle simulations, we investigated the acceleration of suprathermal electrons at a quasi-perpendicular shock studied by Yang et al. (2018), to suggest the importance of shock drift acceleration in the acceleration of electrons. In this paper, using spacecraft observation data analysis and test particle simulations, we expand to study statistically the effect of shock parameters, such as shock-normal angle, upstream Alfvén Mach number, and shock compression ratio, on the ICME-driven shock acceleration efficiency. In addition, the theories for shock acceleration efficiency are derived to compare with observations and simulations. In Section 2, we show the observational data. We describe the numerical model in Section 3 and theoretical models in Section 4. The results of simulations and observations are presented in Section 5. Summary and discussion are given in Section 6.

## 2. OBSERVATIONAL DATA

<sup>1</sup> stream interaction region

From the survey in Yang et al. (2018), 74 ICME-driven shocks are observed by *Wind* over the period from 1995 to 2004. The electron electrostatic analyzer (EESA) in the 3DP instrument (Lin et al. 1995) onboard *Wind* provides three-dimensional (3D) data for eight pitch angle channels in the energy range of  $\sim 3$  eV to  $\sim 30$  keV. For the shock events, the flux data of energetic electrons in the upstream and downstream of the shock (i.e., before and after the shock arrival) can be obtained from the *Wind*/3DP/EESA instrument.

We choose the shock event on 2000 Feb 11 observed by *Wind* as an example. The upstream energy spectra in all pitch angle directions averaged in a period of 10 minutes (23:14 UT–23:24 UT) prior to the shock are plotted in Figure 1, multiplied by  $2^0$ ,  $2^1$ ,  $2^2$ ,  $2^3$ ,  $2^4$ ,  $2^5$ ,  $2^6$ , and  $2^8$  for the pitch angles of  $14^\circ$ ,  $34^\circ$ ,  $56^\circ$ ,  $78^\circ$ ,  $102^\circ$ ,  $124^\circ$ ,  $145^\circ$ , and  $165^\circ$ , respectively. We assume these spectra can be used as the initial upstream electron distribution before the shock acceleration. In this work, we focus on the observations of the electron energy channels at  $\sim 0.634$ ,  $0.920$ ,  $1.339$ ,  $1.952$ ,  $2.849$ , and  $4.161$  keV indicated by  $E_k$  with  $k = 1, 2, 3, \dots, 6$ , and listed in Table 1, from the *Wind*/3DP/EESA measurement. Using the data observed by Magnetic Field Investigation (MFI) (Farrell et al. 1995; Kepko et al. 1996) and Solar Wind Experiment (SWE) (Ogilvie et al. 1995) instruments onboard *Wind* we obtain the upstream average magnetic field  $B_{01} = 7.0$  nT and proton number density  $n_p = 5.19$  cm $^{-3}$ . Thus, the upstream Alfvén speed is  $V_{A1} = 67$  km s $^{-1}$  with the formula  $V_{A1} = B_{01} / \sqrt{\mu_0 n_p m_p}$ , where  $\mu_0$  is space permeability and  $m_p$  is proton mass.

### 3. NUMERICAL MODEL

We study the acceleration of electrons at a plane shock by using spacecraft data analysis and test-particle simulations similar to our previous work (Kong et al. 2017, 2019). Under the given shock parameters, the trajectories of test particles are traced by calculating the motion of equation of particles in the electromagnetic field,

$$\frac{d\mathbf{p}}{dt} = q[\mathbf{E}(\mathbf{r}, t) + \mathbf{v} \times \mathbf{B}(\mathbf{r}, t)], \quad (1)$$

where  $\mathbf{p}$  is the particle momentum,  $q$  is the electron charge,  $\mathbf{v}$  is the particle velocity, and  $t$  is time. The electric field  $\mathbf{E}$  is the convection electric field  $\mathbf{E} = -\mathbf{U} \times \mathbf{B}$ . The shock is located at  $z = 0$ , and the plasma flows from the upstream region with a speed  $\mathbf{U}_1$  to downstream region with a speed  $\mathbf{U}_2$  in the shock reference

frame, as shown in Figure 2. Here,

$$\mathbf{U}_2 = \frac{\mathbf{U}_1}{s}, \quad (2)$$

with shock compression ratio  $s$ . It will be later shown that the downstream fluxes from observations and simulations are measured in the range of  $z$  from 0 to  $z_1 = 2.7 \times 10^{-3}$  au. We assume the plasma speed in the shock transition is in the form (e.g., Qin et al. 2018)

$$U(z) = \frac{U_1}{2s} \left\{ (s+1) + (s-1) \tanh \left[ \tan \left( -\frac{\pi z}{L_{\text{th}}} \right) \right] \right\}, \quad (3)$$

where  $L_{\text{th}}$  is the shock thickness, which is supposed as  $L_{\text{th}} = 2 \times 10^{-6}$  au in this work. It is noted that  $L_{\text{th}}$  is too small to be shown in Figure 2. The magnetic field,  $\mathbf{B}$ , consists of a background field assumed to lie in  $x$ - $z$  plane,  $\mathbf{B}_0$ , and a turbulent field,  $\mathbf{b}$ , composed of a slab and two-dimensional (2D) components,  $\mathbf{b}_{\text{slab}}$  and  $\mathbf{b}_{\text{2D}}$ , respectively (Matthaeus et al. 1990; Mace et al. 2000; Qin et al. 2002a,b)

$$\mathbf{B} = \mathbf{B}_0 + \mathbf{b} = \mathbf{B}_0 + \mathbf{b}_{\text{slab}} + \mathbf{b}_{\text{2D}}. \quad (4)$$

Here, the directions of turbulent magnetic fields  $\mathbf{b}$ ,  $\mathbf{b}_{\text{slab}}$ , and  $\mathbf{b}_{\text{2D}}$  are perpendicular to the direction of the background magnetic field  $\mathbf{B}_0$ .

In all simulations, the slab turbulence has a correlation length of  $\lambda = 0.02$  au. The ratio of slab to 2D correlation length is 2.6 according to previous studies (Osman & Horbury 2007; Weygand et al. 2009, 2011; Dosch et al. 2013). We define the turbulence in a periodic box of size  $[10\lambda, 10\lambda]$  for the 2D component turbulence and size  $25\lambda$  for the slab component turbulence. A dissipation range in which low-energy electrons resonate for the slab turbulence is required, and the break wavenumber is fixed at  $k_b = 10^{-6} \text{ m}^{-1}$  from the slab inertial to dissipation ranges. The spectral indices of the inertial and dissipation ranges are  $\beta_i = 5/3$  and  $\beta_d = 2.7$ , respectively. We take the turbulence level,  $(b/B_0)^2$ , of 0.25 in the upstream and 0.36 in the downstream of the shock. In addition, the energy density ratio of the slab to 2D components is assumed to  $E_{\text{slab}} : E_{\text{2D}} = 20 : 80$ .

In our simulations of shock acceleration of energetic electrons, we use a method of backward tracing electron trajectories (i.e., backward-in-time method, Kong et al. 2017; Kong & Qin 2020). In addition, we vary the parameters, shock-normal angle  $\theta_{Bn}$ , upstream Alfvén Mach number  $M_{A1}$ , and shock compression

ratio  $s$ , indicated as  $i = a, b$ , and  $c$ , respectively, as shown in Table 2. Therefore, for any energy channel we have a total of 315 simulation cases for all possible parameter combinations. Note that the upstream shock speed  $U_1$  can be determined by

$$U_1 = M_{A1} V_{A1}, \quad (5)$$

where the upstream Alfvén speed  $V_{A1}$  is set as  $67 \text{ km s}^{-1}$ . For different shock geometries (from quasi-parallel to quasi-perpendicular shocks) it is shown from the observations in Yang et al. (2018) that there is a downstream enhancement of energetic electrons in the anti-sunward direction, which may come from some beams, but from our simulations in Kong & Qin (2020) we can not get a significant enhancement in this direction. Therefore, in the rest of the paper we only compare the observations and simulations in the perpendicular direction. At the end of the simulation time  $t_{\text{acc}} = 10 \text{ min}$ , the downstream flux in the range  $[z_0, z_1]$  in the  $90^\circ$  pitch angle for a target energy channel is obtained based on the initial upstream distributions as shown in Figure 1, where  $z_0 = L_{\text{th}}/2$  and  $z_1 = V_{\text{sh}}\Delta t \approx 2.7 \times 10^{-3} \text{ au}$  with  $\Delta t = 10 \text{ min}$ . Here, the value of  $z_1$  is set to get a 10-min average flux after the shock crossing. More details about the backward-in-time method are given in Section 3 in Kong & Qin (2020). In addition, different values of the shock parameters, such as shock-normal angle  $\theta_{Bn}$ , upstream Alfvén Mach number  $M_{A1}$ , and compression ratio  $s$  from observations possibly carry unequal weights, i.e., there are more shock events in some values than in other values. Therefore, according to the observations of the 74 shock events listed in Yang et al. (2018), we get a weight function  $W(\theta_{Bn}, M_{A1}, s)$  for each of the 315 simulation cases of the parameter combinations  $(\theta_{Bn}, M_{A1}, s)$ . The input parameters for the shock and turbulence in simulations are summarized in Table 3.

#### 4. THEORETICAL MODELS

If we suppose particles are accelerated by shock drift acceleration, their drift time  $T_{\text{drift}}$  can be written as (Kong & Qin 2020)

$$T_{\text{drift}} = \frac{L_{\text{th}}}{2U_1} + \frac{L_{\text{th}}}{2U_2}. \quad (6)$$

Furthermore, in order to achieve effective acceleration, particles would not move away from the shock thickness within the drift time, i.e.,

$$\frac{1}{2}T_{\text{drift}} v \cos \theta_{Bn} \lesssim L_{\text{th}}, \quad (7)$$

where the factor 1/2 in the left-hand side is used to consider the average over the pitch angle of particle velocity. Therefore, for the critical value  $\cos \theta_{Bn,c}$  with effective acceleration, we have

$$\cos \theta_{Bn,c} = \frac{2L_{th}}{T_{drift}v}. \quad (8)$$

On the other hand, Drury (1983) showed that for each cycle of the particle crossing of the shock front the average momentum change of particles is

$$\begin{aligned} \langle \Delta p \rangle &= 2p \int_0^1 \frac{\mu(U_1 - U_2)}{v} 2\mu d\mu \\ &= \frac{4}{3} \frac{U_1 - U_2}{v} p. \end{aligned} \quad (9)$$

The work done by electric field force is equal to the energy change, i.e.,

$$w = \frac{p\langle \Delta p \rangle}{m}. \quad (10)$$

Substituting Equation (9) into Equation (10), considering Equations (2) and (5), we get

$$w = \frac{4}{3} \left(1 - \frac{1}{s}\right) p M_{A1} V_{A1}. \quad (11)$$

In order for energetic particles to be efficiently accelerated, we can also suppose the work  $w$  is large enough compared with the particle kinetic energy  $E_k$ , i.e.,

$$w \gtrsim \eta E_k, \quad (12)$$

where  $\eta$  is a constant to represent the order of magnitude, which may be taken as 1%. If we substitute Equation (11) into Equation (12) and take an equal sign in the result, we obtain

$$M_{A1} = \frac{3\eta E_k s}{4pV_{A1}(s-1)}, \quad (13)$$

or

$$s = \left(1 - \frac{3\eta E_k}{4pV_{A1}M_{A1}}\right)^{-1}. \quad (14)$$

We suppose Equation (13) can roughly describe the critical value of Mach number  $M_{A1,c}$  with effective acceleration if the compression ratio  $s$  is given by a representative value  $s_r$ , i.e.,

$$M_{A1,c} = \frac{3\eta E_k s_r}{4pV_{A1}(s_r-1)}. \quad (15)$$

Similarly, we suppose Equation (14) can roughly describe the critical value of compression ratio  $s_c$  with effective acceleration if the Mach number  $M_{A1}$  is given by a representative value  $M_r$ , i.e.,

$$s_c = \left(1 - \frac{3\eta E_k}{4pV_{A1}M_r}\right)^{-1}. \quad (16)$$

## 5. RESULTS OF OBSERVATIONAL ANALYSIS AND SIMULATIONS

### 5.1. Stream of energetic particles anti-sunward

According to the previous work by [Yang et al. \(2018\)](#), it is noted that in some SEP events there is a stream of energetic particles in the direction away from the Sun downstream of the shock (see also, [Kong & Qin 2020](#)). Here, we check the universality of this phenomenon. For all the 74 ICME-driven shock events from the data observed by Magnetic Field Investigation (MFI) onboard *Wind* we determine the magnetic field direction by averaging the magnetic field x-component in the GSE coordinate over 10 minutes before and after the shock arrival. Next, with the pitch angle  $\theta$  we define a modified pitch angle  $\theta'$

$$\theta' = \begin{cases} \theta & \text{if magnetic field is sunward,} \\ \pi - \theta & \text{otherwise.} \end{cases} \quad (17)$$

From the data observed by the *Wind*/3DP/EESA measurement, we get the integrated differential intensity  $I_{\theta'}$  over the energy range of 0.634 – 4.161 keV with 10-minute average downstream of the shock for each of the modified pitch angle interval  $\theta'$ . For the 65 out of 74 ICME-driven shock events from [Yang et al. \(2018\)](#), we obtain  $I_0$ ,  $I_{90}$ , and  $I_{180}$  with the modified pitch angle  $\theta'$  nearest to 0°, 90°, and 180°, respectively, and we set  $I_M$  as the maximum of  $I_0$ ,  $I_{90}$ , and  $I_{180}$ . Note that 9 of the 74 shock events are excluded due to bad data in some energy channels. Finally, we define two parameters  $\rho$  and  $\sigma$  as

$$\rho = \frac{I_0}{I_{90}} - \frac{I_{180}}{I_{90}}, \quad (18)$$

and

$$\sigma = \begin{cases} 1 & \text{if } I_0 = I_M, \\ 0 & \text{if } I_{90} = I_M, \\ -1 & \text{otherwise.} \end{cases} \quad (19)$$

Top and bottom panels of Figure 3 show parameter  $\rho$  and  $\sigma$ , respectively, versus the shock-normal angle  $\theta_{Bn}$  for the 65 ICME-driven shock events with black circles. The red circles of the top and bottom panels

indicate the average  $\rho$  and  $\sigma$  in each shock normal angle interval. From the figure we can see that for most of the ICME-driven shock events there is a stream of energetic particles away from the Sun downstream of the shock. Therefore, in the following, we only study the acceleration of energetic particles in  $90^\circ$  pitch angle with observations and simulations in order to avoid the stream of particles in observations.

### 5.2. Sample of SEPs with ICME-driven shocks with observations and simulations

In order to show the shock acceleration we select four sample observed SEP events from the 74 events with ICME-driven shocks listed in Yang et al. (2019). In Figure 4 red and black circles indicate downstream and upstream fluxes in  $90^\circ$  pitch angle, respectively, for the four observed shock events in the energy range of 0.634–4.161 keV, averaged over a period of 10 minutes. Each panel of the figure shows an event, with the date, shock-normal angle, compression ratio, and Alfvén Mach number listed in the lower left corner. From the figure we can see that for all the observed events downstream fluxes are larger than the upstream ones, and there is significant shock acceleration of energetic particles.

Furthermore, for each of the 315 simulation cases of the parameter combinations  $(\theta_{Bn}, M_{A1}, s)$ , we perform simulations with 10,000 test particles using the backward-in-time method with the upstream flux from observations as the initial condition to get the downstream flux for each of the energy channels  $E_k$ . We select four sample simulation cases to show the simulation results. In Figure 5 red circles indicate downstream flux from simulations in  $90^\circ$  pitch angle for the four cases in the energy range of 0.634–4.161 keV, and black circles show the initial distribution using a 10-min average upstream flux observed on 2000 Feb 11. Similar as Figure 4, each panel of Figure 5 shows a simulation case, with the shock normal angle, compression ratio, and Alfvén Mach number listed in the lower left corner. We can see that, for all the four cases, simulated downstream fluxes are larger than the upstream one which is used as the source for the simulations, and there is significant shock acceleration of particles in the simulations.

From the sample of observations and simulations, it may be suggested that, generally, as shock normal angle increases from parallel to perpendicular, shock acceleration efficiency increases. In addition, one may assume that, with similar shock normal angle, shock acceleration efficiency increases with the increase of compression ratio and Alfvén Mach number.

### 5.3. Shock acceleration efficiency from observations and simulations

In order to further study the shock acceleration efficiency, for the 74 observational shock events we obtain the ratio,  $R_a$ , between downstream and upstream flux for  $90^\circ$  pitch angle in each of the energy channels  $E_k$  listed in Table 1. If  $R_a$  is larger than a threshold value  $R_t$ , which is set to 4 in this paper, we suppose the shock acceleration is effective. Therefore, we can study the shock acceleration efficiency depending on the shock normal angle  $\theta_{Bn}$ , the upstream Alfvén Mach number  $M_{A1}$ , and compression ratio  $s$  from observations. First, we divide the shock normal angle into different intervals, in each of which we obtain the ratio  $N_1/N_0$ , with the number of shock events with high acceleration efficiency  $N_1$  and the total number of shock events  $N_0$ . Similarly, we divide the upstream Alfvén Mach number  $M_{A1}$  and compression ratio  $s$  to obtain the ratio  $N_1/N_0$  for  $M_{A1}$  and  $s$ , respectively.

Furthermore, using the ratio,  $R_a$ , between the downstream flux from simulations and the upstream flux we can determine that the acceleration of the shock with the condition  $(\theta_{Bn}, M_{A1}, s)$  is effective if  $R_a > R_t$ . In this way, we can study the shock acceleration efficiency depending on  $\theta_{Bn}$ ,  $M_{A1}$ , and  $s$  from simulations. Since different values of the shock parameters, such as  $\theta_{Bn}$ ,  $M_{A1}$ , and  $s$  from observations carry different weights, here we have to consider the weight  $W(\theta_{Bn}, M_{A1}, s)$  for their contribution to the number  $N_1$  and  $N_0$ . We divide the shock normal angle into different intervals, for each of which we calculate the ratio  $N_1/N_0$ . Similarly, we can divide  $M_{A1}$  and  $s$  into different intervals to calculate the ratio  $N_1/N_0$  depending on  $M_{A1}$  and  $s$ , respectively.

Figure 6 shows the ratio  $N_1/N_0$  versus the shock normal angle cosine  $\cos \theta_{Bn}$  (left panel), upstream Alfvén Mach number  $M_{A1}$  (middle panel), and compression ratio  $s$  (right panel) in the energy channel of 0.634 keV for the simulations (asterisks) and observations (circles). Note that we use  $x_i$  with  $i = a, b$ , and  $c$  to indicate shock normal angle cosine  $\cos \theta_{Bn}$ , upstream Alfvén Mach number  $M_{A1}$ , and compression ratio  $s$ , respectively. Figure 6(a) shows that for both the observations and simulations, with  $\cos \theta_{Bn} \sim 0$ , i.e., quasi-perpendicular geometry, the ratio  $N_1/N_0$  is the highest, and it decreases with the increase of the shock normal angle cosine  $\cos \theta_{Bn}$ , which indicates that the acceleration of particles is more efficient at quasi-perpendicular shocks. On the other hand, Figures 6(b) and (c) show that for both the observations and simulations the ratio  $N_1/N_0$  increases with the increase of upstream Alfvén Mach number  $M_{A1}$  (panel b),

and compression ratio  $s$  (panel c), which indicates that the acceleration efficiency enhances with the increase of upstream Alfvén Mach number and compression ratio, respectively.

Actually, one may fit both the data from the observations and simulations to a function

$$y = \frac{1}{1 + \left(\frac{x_i}{\xi_i}\right)^{d_i}}, \quad (20)$$

where  $\xi_i$  is the fit factor,  $d_i = 1/2$ ,  $-2$ , and  $-2$ , with  $i = a$ ,  $b$ , and  $c$ . The positive and negative  $d_i$  make the function decreasing and increasing, respectively. The fit factor  $\xi_i$  in Equation (20), in fact, represents a critical value for efficient acceleration, i.e.,  $\cos \theta_{Bn,c}$ ,  $M_{A1,c}$ , and  $s_c$ , in each energy channel  $E_k$  where the ratio  $N_1/N_0$  is as large as 1/2. We assume that if  $\cos \theta_{Bn} \lesssim \cos \theta_{Bn,c}$ ,  $M_{A1} \gtrsim M_{A1,c}$ , or  $s \gtrsim s_c$ , the shock acceleration efficiency is significant. In Figure 6 the red and black dashed curves indicate the fits to the data from observations and simulations, respectively. It is shown that the fitting results can roughly give the trends of the observations and simulations.

Figure 7 shows similar plots to Figure 6, except in the energy channel of 0.920 keV. In Figure 7, both the simulations (asterisks) and observations (circles) show that the ratio of event numbers with the high shock acceleration efficiency,  $N_1/N_0$ , decreases with the shock normal angle cosine, and increases with the upstream Alfvén Mach number, and compression ratio. However, it is shown that the ratio  $N_1/N_0$  is smaller in the energy of 0.920 keV than 0.634 keV, which suggests that low-energy electrons are more easily to be accelerated. For all other energy channels listed in Table 1 we have similar results (not shown). The fit factors  $\xi_i$  for all energy channels are listed in Tables 4 and 5 for data from observations and simulations, respectively. Although the fitting result can only roughly show the trends of the data, the values of fit factors  $\xi_i$  with  $i = a$ ,  $b$ , and  $c$ , i.e., the critical values for efficient acceleration, i.e.,  $\cos \theta_{Bn,c}$ ,  $M_{A1,c}$ , and  $s_c$ , respectively, are useful to determine the shock acceleration efficiency.

Figure 8 shows critical values of shock normal angle cosine  $\cos \theta_{Bn,c}$  (upper panel) and the corresponding shock normal angle  $\theta_{Bn,c}$  (lower panel) in each of the energy channels  $E_k$  for both the observations (red circles) and simulations (black asterisks). We can see that, with the increase of electron energy, the critical shock normal angle cosine (upper panel) decreases and the critical shock normal angle (lower panel) increases, which suggests that higher energy electrons are more difficult to be accelerated by shocks. In

addition, the critical angle is very close to  $90^\circ$  for higher energy channels. One should note that for the two highest energy channels the values of critical angle from observational data are not available since the proper fitting results of the observational data to Equation (20) are not obtained. It is shown that, the fit curve of the critical shock normal angle from simulations generally agrees with that from observations. However, in lower energy, the critical shock normal angles from simulations are higher than those from observations. It is suggested that our simulations show less shock acceleration than observations in lower energy electrons. Furthermore, blue curves of the theoretical results from Equation (8) suggest that the theoretical critical shock normal angle has similar trends of that from both observations and simulations.

Figure 9 shows critical values of the upstream Alfvén Mach number  $M_{A1,c}$  (upper panel) and compression ratio  $s_c$  (lower panel) versus the electron energy for both the observations (red circles) and simulations (black asterisks). From the upper panel of Figure 9 it is noted that for the two highest energy channels the critical values of the upstream Alfvén Mach number from simulations are not available because the proper fitting results are not obtained. The figure shows both of the critical upstream Alfvén Mach number and the critical compression ratio increase with the electron energy for both observations and simulations. Furthermore, for both of  $M_{A1,c}$  and  $s_c$  we can see that the simulation results generally agree with the observational ones. Using Equations (15) and (16), also shown in Figure 9 are the theoretical results for the critical values with effective shock acceleration. It is noted that in Equations (15) and (16)  $\eta$  is taken as 1%, the theoretical results also depend on the values of free parameters  $s_r$  and  $M_r$ , which are set to 1.3 and 2.5, respectively, here, to make the theories fit better with the observations and simulations. However, we can still suggest that the theories show similar trends of observations and simulations.

## 6. SUMMARY AND DISCUSSION

We study the shock acceleration efficiency of suprathermal electrons, with spacecraft observational data for many ICME-driven shock events and test-particle simulations for cases of different parameters. It is suggested by Yang et al. (2018) (see also, Kong & Qin 2020) that there exists a stream of energetic particles anti-sunward downstream of the shock in some SEP events. We check the 74 ICME-driven shock events listed in Yang et al. (2019), and find that for the 65 events with complete data there mostly exists a stream of energetic particles anti-sunward downstream of the shock. Therefore, in this paper, we only study the shock

acceleration efficiency of energetic particles in 90° pitch angle with both observations and simulations. In addition, we develop a theory for the value of critical shock normal angle  $\theta_{Bn,c}$  with high efficiency of shock acceleration, assuming shock drift acceleration of particles. We also obtain theories for the critical values of Mach number  $M_{A1,c}$  and compression ratio  $s_c$  with effective acceleration, based on the average momentum change of particles suggested by [Drury \(1983\)](#) for each cycle of the particle crossing of the shock front.

For the 74 shock events listed in [Yang et al. \(2019\)](#), we use data analysis on the spacecraft observations in energy channels ranging from 0.634 keV to 4.161 keV, to study the shock acceleration efficiency depending on different shock parameters, including shock-normal angle  $\theta_{Bn}$ , upstream Alfvén Mach number  $M_{A1}$ , and compression ratio  $s$ . In addition, we perform the similar research using 315 test-particle simulation cases in different conditions of shock parameters. With both the observational data and simulation results, we obtain the ratio  $N_1/N_0$  of the events with the large ratio  $R_a$ , i.e.,  $R_a > R_t$  (the threshold value  $R_t$  set to 4 here), between the downstream flux to the background one. It is noted that, in order to obtain the ratio  $N_1/N_0$ , the weights of the individual simulation cases are considered since different values of the shock parameters carry different weights according to the observations. We find that for both observations and simulations, the ratio  $N_1/N_0$  decreases with the increase of shock-normal angle cosine and increases with upstream Mach number and compression ratio, indicating that a large shock angle, Mach number, and compression ratio can help improve the shock acceleration efficiency. Furthermore, the variations of  $N_1/N_0$  with shock parameters are fitted with functions to obtain the critical values with effective shock acceleration. It is shown that the critical parameters,  $\theta_{Bn,c}$ ,  $M_{A1,c}$ , and  $s_c$ , with effective shock acceleration from observations and simulations are somehow in agreement, and they have similar trends of the theoretical results. Therefore, we suggest that shock drift acceleration is efficient in the electron acceleration by ICME-driven shocks ([Yang et al. 2018, 2019; Kong & Qin 2020](#)). However, it is also shown that, our simulations have weaker acceleration efficiency than the observations, especially for lower and higher energy electrons. In addition, our simulation results are less smooth than the observations.

It is noted that, limited by the computing resources, the upper limit of slab turbulence wavenumbers in the simulations is set to  $k \sim 1.75 \times 10^{-4} \text{ m}^{-1}$ , however, for low energy electrons, which is not significantly larger than the minimum resonant wavenumber,  $k_{rm} = eB_0/p_e$ , where  $p_e$  is the electron momentum. For

example, for 0.634-keV electrons,  $k_{rm} \sim 8 \times 10^{-5} \text{ m}^{-1}$ . Therefore, in our simulations lower energy electrons have narrow resonant range in the spectrum of turbulence compared to the observations. This might be the reason why we get weak acceleration efficiency in low energy electrons in the simulations compared to the observations. In addition, the lower energy electrons accelerated by a shock may be further accelerated to higher energy. Therefore, the weak acceleration of lower energy electrons because of the narrow resonant range would also cause the weak acceleration for higher energy electrons. Furthermore, the simulations of the acceleration of high energy electrons, which have a large velocity, need more computing resources in order to ensure numerical accuracy. We will use more powerful computation resources to improve the computation accuracy and increase the upper limit of the slab turbulence in the simulations in future works, so that we can get more effective shock acceleration.

#### ACKNOWLEDGMENTS

This work was supported, in part, under grants NNSFC 42074206 and NNSFC 41874206. The work was carried out at National Supercomputer Center in Tianjin, and the calculations were performed on TianHe-1 (A).

#### REFERENCES

Axford, W. I., Leer, E., & Skadron, G. 1977, Proc. ICRC (Plovdiv), 11, 132

Bell, A. R. 1978, MNRAS, 182, 147

Bieber, J. W., Wanner, W., & Matthaeus, W. H. 1996, J. Geophys. Res., 101, 2511

Blandford, R. D., & Ostriker, J. P. 1978, ApJL, 221, L29

Dosch, A., Adhikari, L., & Zank, G. P. 2013, in 13th Int. Solar Wind Conf. (Solar Wind 13), 1539, 155

Dresing, N., Theesen, S., Klassen, A.,

Drury, L. O'C. 1983, Rep. Prog. Phys., 46, 973 & Heber, B. 2016, A&A, 588, A17

Farrell, W. M., Thompson, R. F., Lepping, R. P., & Byrnes, J. B. 1995, IEEE Trans. on Magnetics, 31, 966

Guo, F., & Giacalone, J. 2012, ApJ, 753, 28

Kepko, E. L., Khurana, K. K., Kivelson, M. G., et al. 1996, IEEE Transactions on Magnetics, 32, 2

Klassen, A., Bothmer, V., Mann, G., et al. 2002, A&A, 385, 1078

Kong, F. J., Qin, G., & Zhang, L. H. 2017, ApJ, 845, 43

Kong, F.-J., Qin, G., Wu, S.-S., Zhang, L.-H., Wang, H.-N., Chen, T., & Sun, P. 2019, ApJ, 877, 97

Kong, F. J., & Qin, G. 2020, ApJ, 896, 20

Krymsky, G. F. 1977, *DoSSR*, 234, 1306

Lin, R. P., Anderson, K. A., Ashford, S., et al. 1995, *SSRv*, 71, 125

Mace, R. L., Matthaeus, W. H., & Bieber, J. W. 2000, *ApJ*, 538, 192

Mann, G., Aurass, H., & Warmuth, A. 2006, *A&A*, 454, 969

Mann, G., Classen, H. T., & Motschmann, U. 2001, *J. Geophys. Res.*, 106, 25323

Matthaeus, W. H., Goldstein, M. L., & Roberts, D. A. 1990, *J. Geophys. Res.*, 95, 20673

Miteva, R., & Mann, G. 2007, *A&A*, 474, 617

Ogilvie, K. W., Chornay, D. J., Fritzenreiter, R. J., et al. 1995, *SSRv*, 71, 55

Osman, K. T., & Horbury, T. S. 2007, *ApJL*, 654, L103

Qin, G., Matthaeus, W. H., & Bieber, J. W. 2002a, *Geophys. Res. Lett.*, 29, 1048

Qin, G., Matthaeus, W. H., & Bieber, J. W. 2002b, *ApJ*, 578, L117

Qin, G., Kong, F. J., & Zhang, L. H. 2018, *ApJ*, 860, 3

Saito, S., & Umeda, T. 2011, *ApJ*, 736, 35

Tsuneta, S., & Naito, T. 1998, *ApJL*, 495, L67

Warmuth, A., Mann, G., & Aurass, H. 2009, *A&A*, 494, 677

Weygand, J. M., Matthaeus, W. H., Dasso, S., et al. 2009, *J. Geophys. Res.*, 114, A07213

Weygand, J. M., Matthaeus, W. H., Dasso, S., & Kivelson, M. G. 2011, *J. Geophys. Res.*, 116, A08102

Yang, L., Wang, L., Li, G., et al. 2018, *ApJ*, 853, 89

Yang, L., Wang, L., Li, G., et al. 2019, *ApJ*, 875, 104

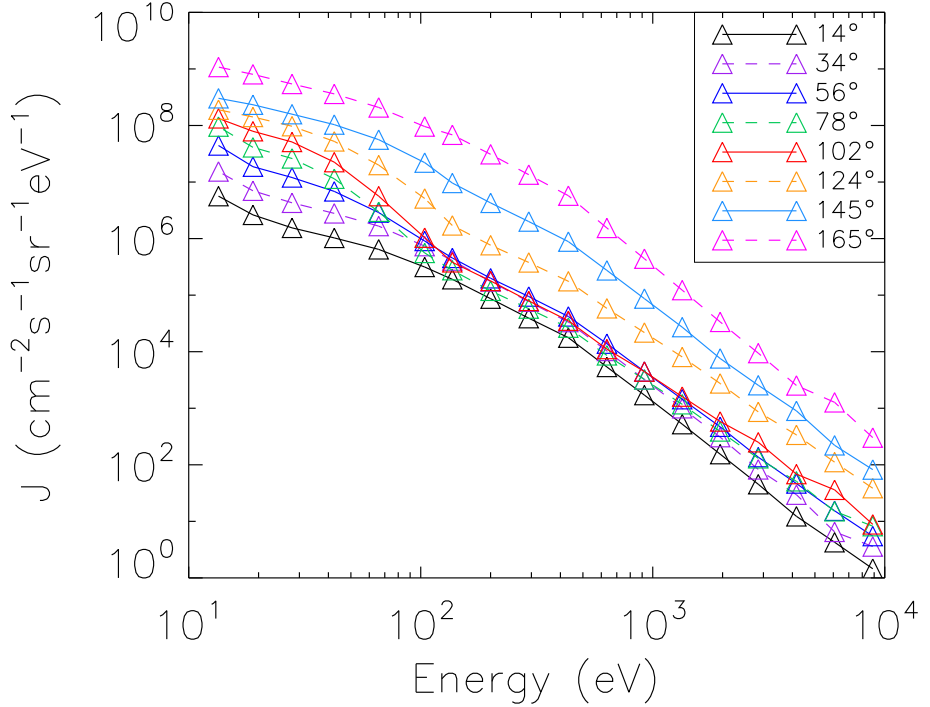


**Figure 1.** Initial upstream electron energy spectra for eight pitch angle channels denoted with different color triangles by averaging the flux data on *Wind*/3DP ahead of the shock in a period of 10 minutes. Note that the spectra with pitch angles of  $14^\circ$ ,  $34^\circ$ ,  $56^\circ$ ,  $78^\circ$ ,  $102^\circ$ ,  $124^\circ$ ,  $145^\circ$ , and  $165^\circ$  are multiplied by  $2^0$ ,  $2^1$ ,  $2^2$ ,  $2^3$ ,  $2^4$ ,  $2^5$ ,  $2^6$ , and  $2^8$ , respectively.

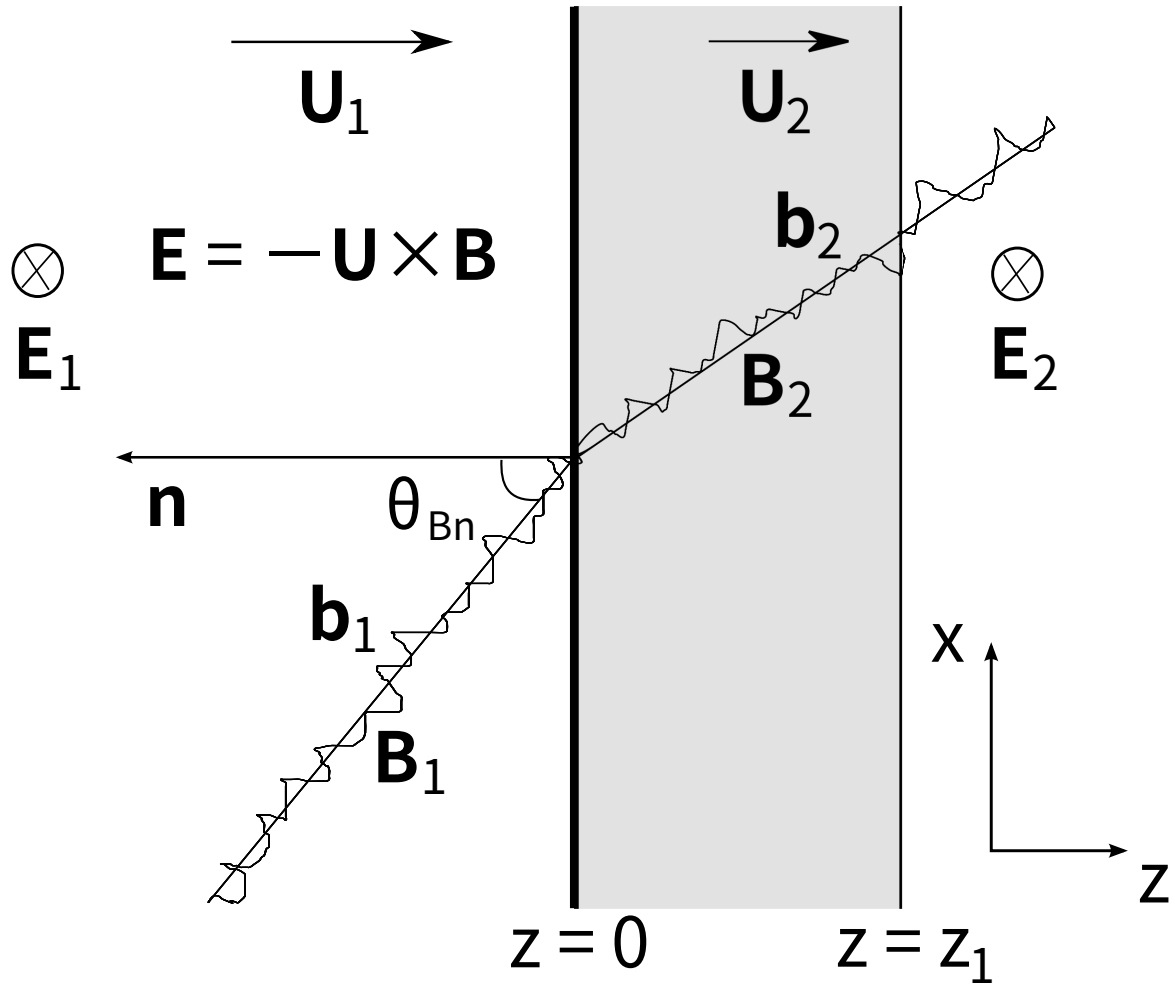


**Figure 2.** The schematic diagram for the shock geometry. The shock plane is located at  $z = 0$ , and the downstream fluxes from observations and simulations are measured in the range of  $z$  from 0 to  $z_1$ . Note that the shock thickness is not shown.

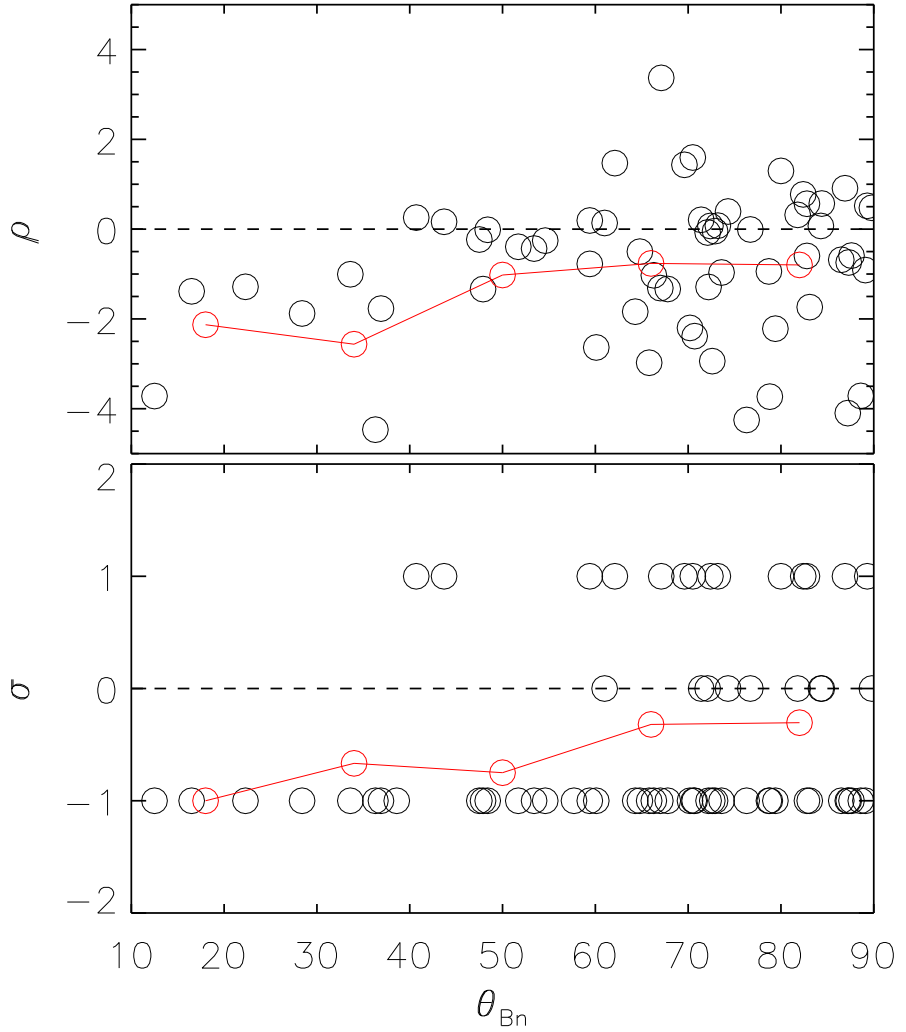


**Figure 3.** Top and bottom panels show parameters  $\rho$  and  $\sigma$ , respectively, versus the shock-normal angle  $\theta_{Bn}$  for 65 shock events with black circles. The red circles in top and bottom panels indicate the average  $\rho$  and  $\sigma$ , respectively, in each shock normal angle interval.

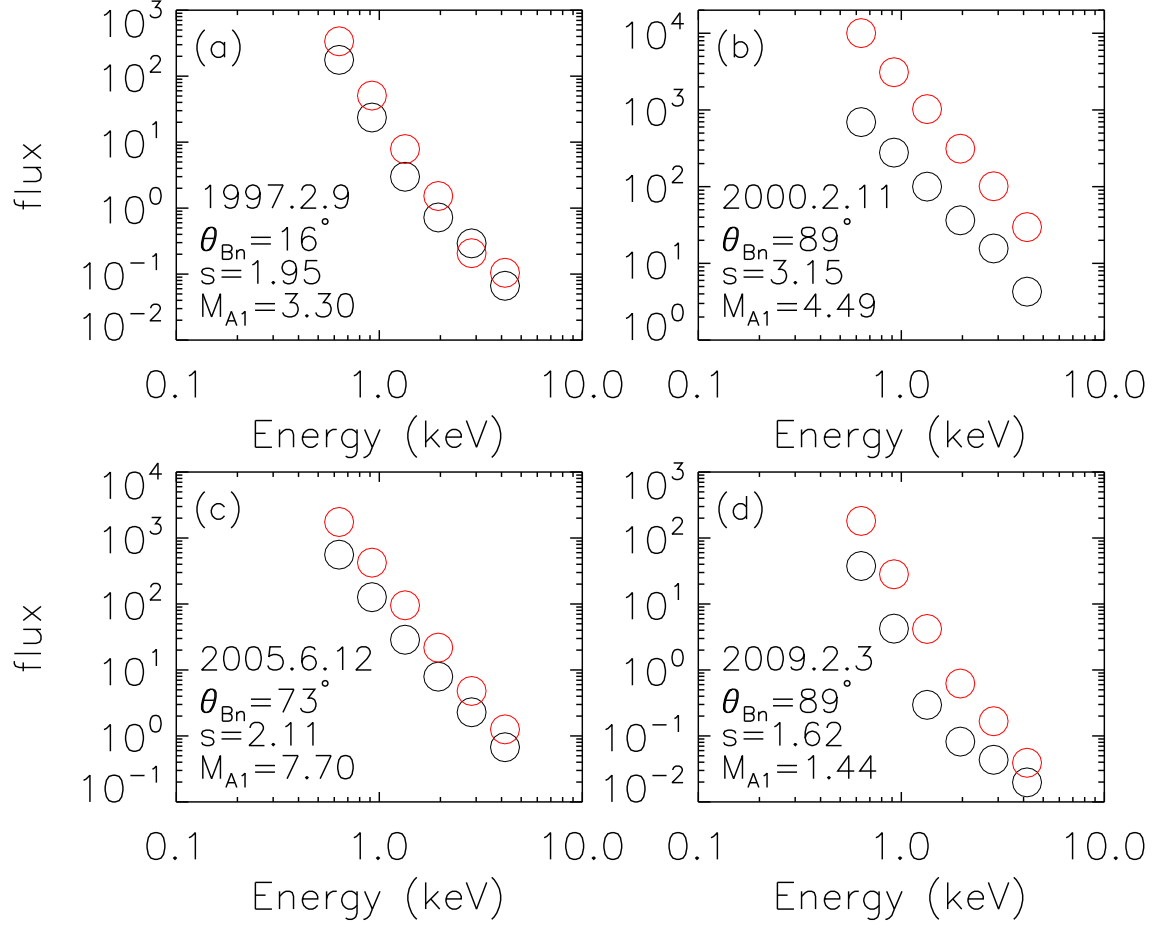


**Figure 4.** Downstream flux (red circles) and upstream flux (black circles) for four sample observed shock events in the energy range of 0.634 – 4.161 keV. Note that the upstream and downstream flux are averaged over a period of 10 minutes. The date, shock-normal angle, compression ratio, and Alfvén Mach number of each shock event are listed in the lower left corner.

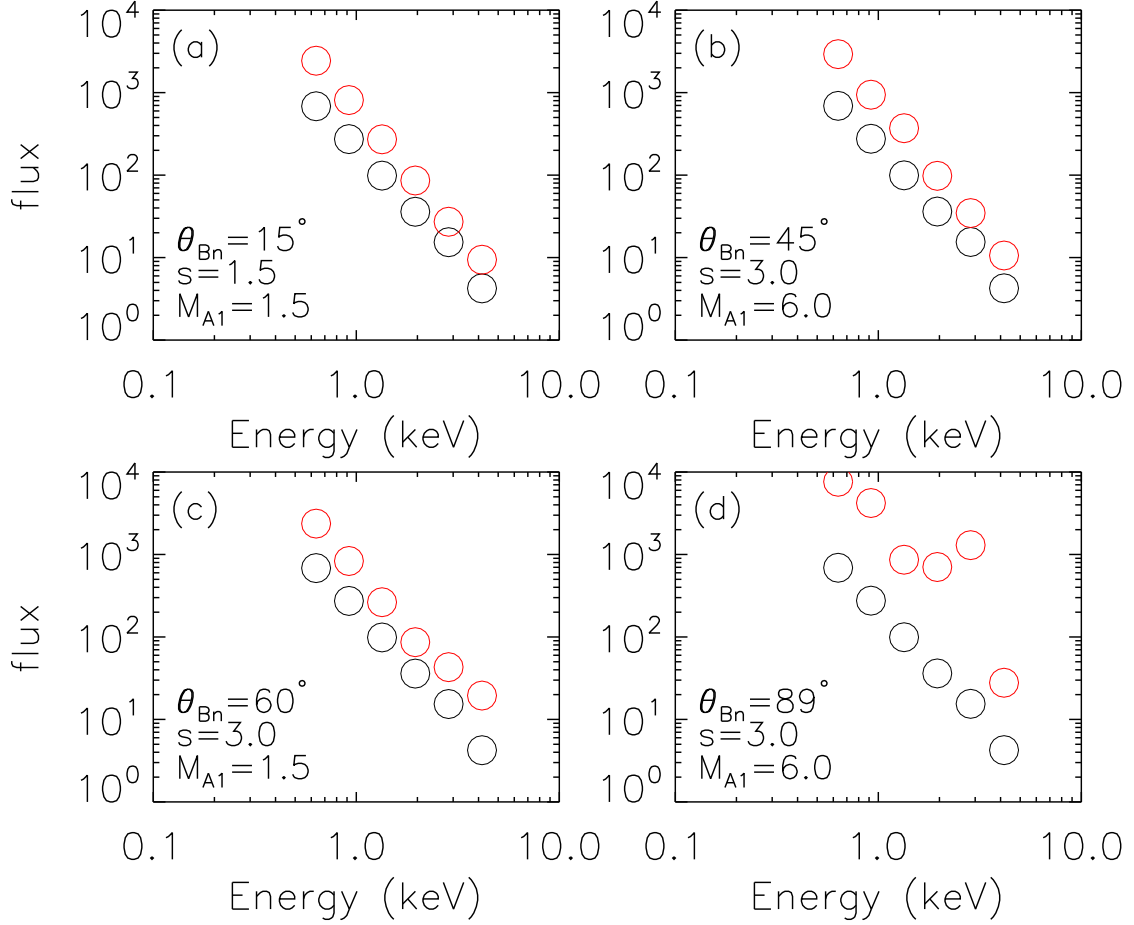


**Figure 5.** Downstream flux (red circles) for four sample simulation cases in the energy range of 0.634–4.161 keV with the source (black circles) from the observed 10-min average upstream flux on 2000 Feb 11. The shock-normal angle, compression ratio, and Alfvén Mach number for each case are listed in the lower left corner.

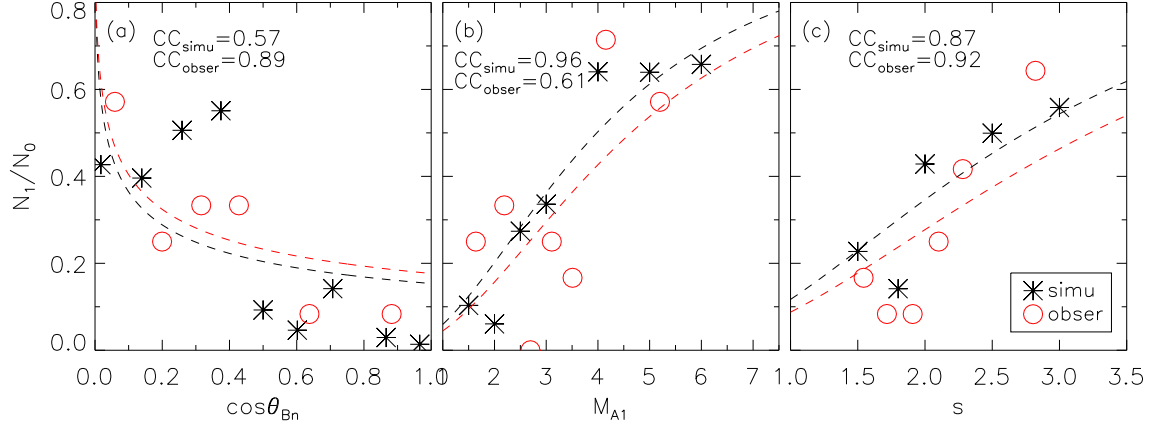


**Figure 6.** Ratio of event numbers  $N_1/N_0$  versus the shock normal angle cosine  $\cos \theta_{Bn}$  (left panel), upstream Alfvén Mach number  $M_{A1}$  (middle panel), and compression ratio  $s$  (right panel) in the energy channel of 0.634 keV for the simulations (asterisks) and observations (circles), with the threshold value  $R_t = 4$  for the downstream to upstream flux ratio. The red (black) dashed curves indicate fits to the data from observations (simulations). The quantity  $CC$  denotes the linear coefficient between the data (asterisks or circles) and the values calculated on the fit curve.

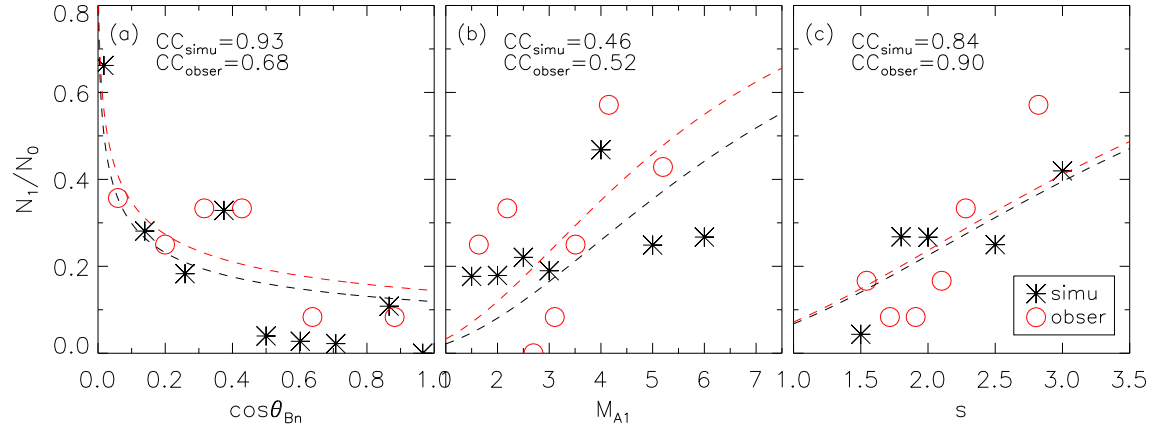


**Figure 7.** Same as Figure 6, except that the energy channel is 0.920 keV.

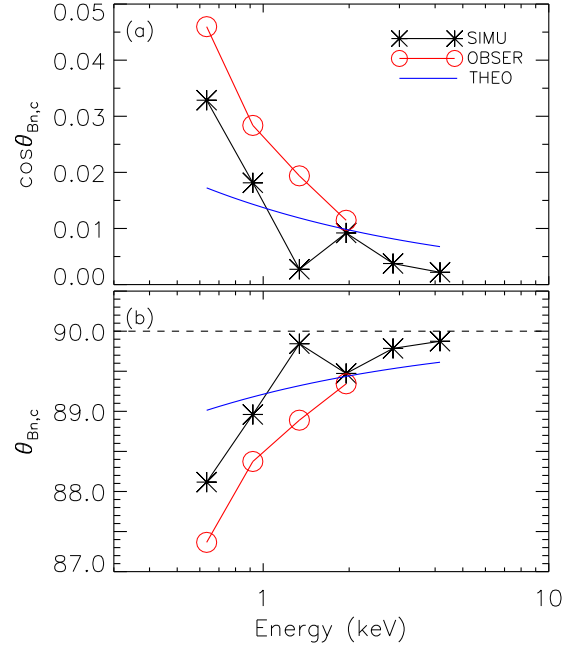


**Figure 8.** Critical values of the shock-normal angle cosine  $\cos \theta_{Bn,c}$  (upper panel) and shock-normal angle  $\theta_{Bn,c}$  (lower panel) versus the electron energy channel. The black asterisks and red circles correspond to the results from the simulations and observations, respectively. The blue curve is the theoretical result of critical values using Equation (8).

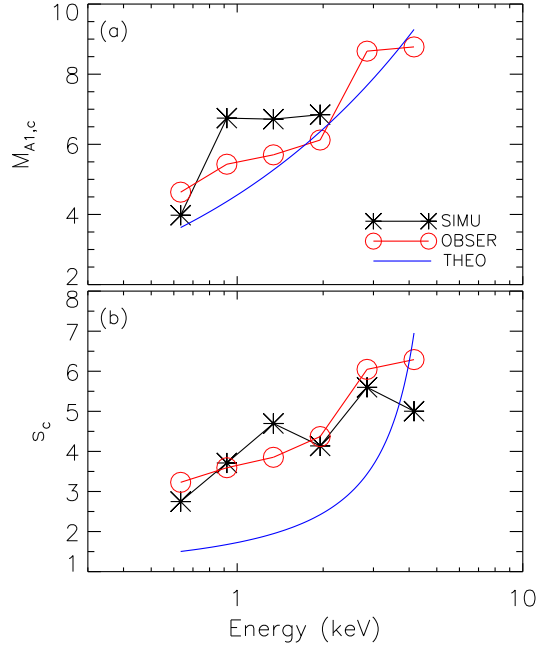


**Figure 9.** Critical values of upstream Alfvén Mach number  $M_{A1,c}$  (upper panel) and compression ratio  $s_c$  (lower panel) versus the electron energy channel. The black asterisks and red circles correspond to the results from the simulations and observations, respectively. The theoretical results of critical values using Equation (15) and Equation (16) are plotted with blue curves in the upper and lower panels, respectively.

**Table 1.** Energy channels  $E_k$ 

$k$	1	2	3	4	5	6
$E_k$ (keV)	0.634	0.920	1.339	1.952	2.849	4.161

**Table 2.** Parameter values for Different Simulation Cases

Parameter	Values
$\theta_{Bn}$	$15^\circ, 30^\circ, 45^\circ, 53^\circ, 60^\circ, 68^\circ, 75^\circ, 82^\circ, 89^\circ$
$M_{A1}$	1.5, 2.0, 2.5, 3.0, 4.0, 5.0, 6.0
$s$	1.5, 1.8, 2.0, 2.5, 3.0

**Table 3.** Input Parameters for the Shock and Turbulence

Parameter	Description	Value
$V_{\text{sh}}$	shock speed	682 km s <sup>-1</sup>
$B_{01}$	upstream magnetic field	7.0 nT
$L_{\text{th}}$	shock thickness	2×10 <sup>-6</sup> au
$V_{\text{A1}}$	upstream Alfvén speed	67 km s <sup>-1</sup>
$\lambda$	slab correlation length	0.02 au
$\lambda_x$	2D correlation length	$\lambda/2.6$
$E_{\text{slab}} : E_{\text{2D}}$	two-component energy density ratio	0.25
$(b/B_0)^2_1$	upstream turbulence level	0.25
$(b/B_0)^2_2$	downstream turbulence level	0.36
$k_b$	break wavenumber	10 <sup>-6</sup> m
$\beta_i$	inertial spectral index	5/3
$\beta_d$	dissipation spectral index	2.7

**Table 4.** Fit Factors for Observations of Energy Channels  $E_k$  Listed in Table 1

$\xi_i$	$k$	1	2	3	4	5	6
$i$							
a		0.0460	0.0284	0.0194	0.0115	0.00185	0.00136
b		4.64	5.43	5.70	6.12	8.66	8.78
c		3.23	3.59	3.85	4.37	6.05	6.29

**Table 5.** Fit Factors for Simulations of Energy Channels  $E_k$  Listed in Table 1

$\xi_i$	$k$	1	2	3	4	5	6
a		0.0329	0.0181	0.00273	0.00921	0.00375	0.00219
b		3.98	6.75	6.72	6.84	12.0	9.44
c		2.75	3.71	4.70	4.14	5.60	5.00